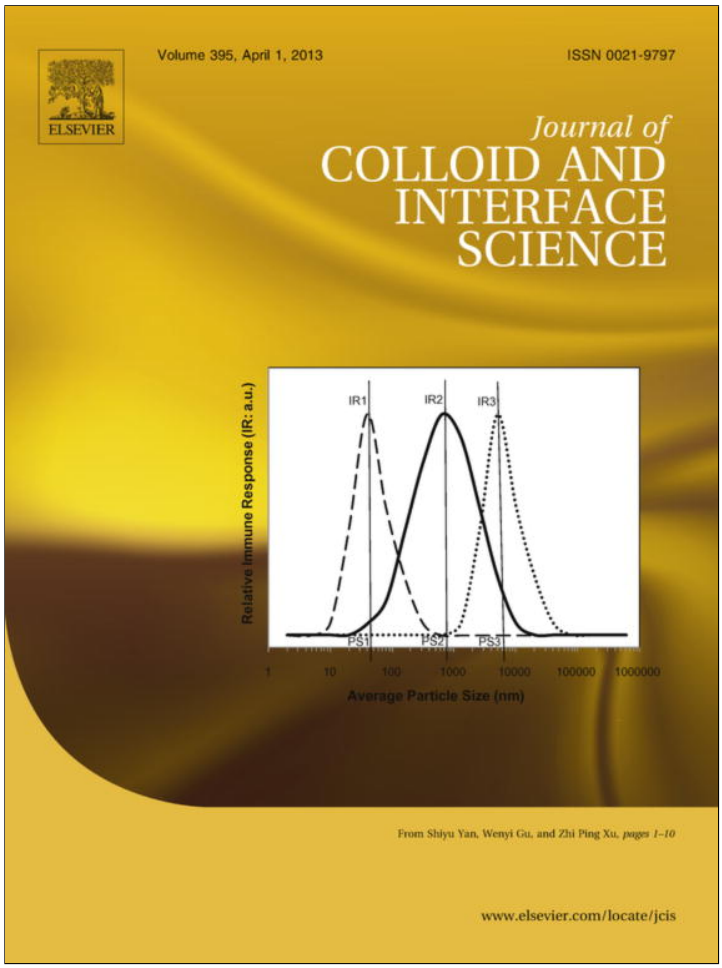

Journal of Colloid and Interface Science 395 (2013) 263–268

Contents lists available at SciVerse ScienceDirect

Journal of Colloid and Interface Science

www.elsevier.com/locate/jcis

Direct observation of concentration profiles induced by drying of a 2D colloidal dispersion drop

F. Giorgiutti-Dauphiné, L. Pauchard *

Univ. Pierre et Marie Curie-Paris6, Univ. Paris-Sud, CNRS, Lab FAST, Bat. 502, Campus Univ., Orsay F-91405, France

ARTICLE INFO

Article history:
Received 13 October 2012
Accepted 9 November 2012
Available online 11 December 2012

Keywords:
Drying
Colloidal
Diffusion
Interface

ABSTRACT

We report experimental results on the drying of a colloidal dispersion drop in a circular thin cell. This confined geometry is well adapted to quantify concentration profiles inside the drop using fluorescence microscopy. Two stages have been identified in the drop evolution. In the first one the drop is shrinking such as if a pure drop, keeping axisymmetry. In the second one strong distortions occur and result in the appearance of a local depression at the drop surface. This process results in the spontaneous formation of a complex drop shape with both concave and convex interfaces. The influence of the interface concavity on the concentration profiles inside the drop and the drying kinetics are investigated. Particularly, concentration profiles are related to the nonuniform evaporation rate at the distorted drop surface.

1. Introduction

Most coatings are made by depositing on a substrate a volatile liquid that contains dispersed colloidal particles or dissolved macromolecules. The liquid is then evaporated until a dry film is obtained. The success of the coating procedure is crucial and confers new functionalities to the coating material such as mechanical or chemical protection, optical or electrical properties. Common examples are paints, coatings colors for paper or anticorrosion coatings for steel. For such applications drying techniques have been developed in order to achieve a good control of the properties of the final film such as thickness, density and structure. Yet concerning the deposition of dispersions of nanometric particles, there are basic problems that prevent further technical advances. These problems have their origins in phenomena that take place at different stages of the film formation process. Also, during evaporation, the film composition evolves and starts from a gas of particles to finally reach a solid like phase with the formation of a gel. Particularly, evaporation at the free surface creates a concentration gradient of the non-volatile species across the film thickness. These concentration gradients can have other possible sources such as Rayleigh–Bénard or Bénard–Marangoni instabilities due to temperature or/and surface tension gradients [1–4]. Also mechanical instability can occur when a skin forms at the surface [5–9], resulting in spatial variations of the liquid–air interface; in turn this affects the evaporation process, and consequently the diffusion in the film. Here we consider experimental conditions where the system is stable regarding to hydrodynamic instabilities but unstable regarding to mechanical instabilities. The geometry is a drop sandwiched between two parallel circular glass slides (Fig. 1). In this quasi-2D geometry, the evaporation flux is radial and accumulation of non-volatile species at the liquid/air interface results in the formation of a skin at the drop edge. This setup is well adapted to observe and quantify concentration profiles inside the liquid drop using fluorescence microscopy. Notably, strong deformations of the drop interface can induce concave and convex interfaces [10–12]. By means of fluorescence microscopy, the distribution of particles in the drop volume is characterized. These measurements have been related to the evaporation rate through the concave and convex air/drop interfaces.

2. Experimental

2.1. Materials

Two colloidal systems have been studied.

The first is an aqueous dispersion of fluorescent particles, 20 nm diameter, made of polymethylmethacrylate (provided by Micromod). The particle volume fraction is initially 5% (polydispersity <0.2). The mass density of the particles is 1.03 g cm^{-3}. They are characterized by an absorbance: $\lambda_{excitation} = 475$ nm and an emission: $\lambda_{emission} = 510$ nm. The initial viscosity of the dispersion is $\eta = 5$ mPa s (measurements using a rheometer Contraves LS30) and the surface tension is equal to 65 ± 5 mN m^{-1} (measurements using the Wilhelmy plate method). This system has been studied in two cases: (i) without any additional compounds and (ii) as probes

* Corresponding author.
E-mail addresses: fred@fast.u-psud.fr (F. Giorgiutti-Dauphiné), pauchard@fast.u-psud.fr (L. Pauchard).

0021-9797/$ - see front matter © 2012 Elsevier Inc. All rights reserved.
http://dx.doi.org/10.1016/j.jcis.2012.11.019

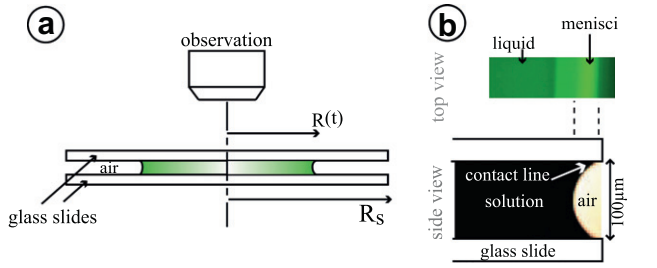

Fig. 1. (a) Set-up in side view: a droplet of solution (radius $R(t)$) is sandwiched between two circular glass slides (radius R_s). (b) Images of a meniscus at the drop edge in top view and in side view (contact angles of the liquid on the two glass slides $\sim 38^\circ$).

when added to an aqueous dispersion of nanolatex particles (see below).

The second system is an aqueous dispersion of nanolatex particles, 25 nm diameter, made of polystyrene (provided by Rhodia Recherche, Aubervilliers, France). The glass transition temperature is around 100°C; consequently at room temperature the nanolatex particles are assumed to be rigid (not deformable). The particle volume fraction is initially 24% and stabilization is feasible due to the presence of surfactants (SDS) [13]. The Debye screening length is 55 nm. The weak polydispersity of the particles (polydispersity ~0.18) prevents from crystallization. The mass density of the particles is 1.05 g.cm$_{-3}$. The initial viscosity of the dispersion is η = 8 mPa s (measurements using a rheometer Contraves LS30) and the surface tension is equal to 62 ± 5 mN m^{-1} (measurements using the Wilhelmy plate method).

When fluorescent probes are added to the Latex dispersion, the ratio of fluorescent probes is chosen to optimize the fluorescence intensity profile (see Section 2.2).

2.2. Methods

The confined geometry consists of a thin cell made of two circular, parallel and horizontal glass slides of radius R_s (Fig. 1a) [16]: in our experiments $R_s = 10$ mm. The slides are carefully cleaned then lubricated with a thin film of silicon oil $V1000$ (viscosity 1 Pa s) spread, then carefully wiped. This treatment prevents the pinning process of the drop contact line [11]. A drop of the dispersion is placed on the bottom substrate with a micropipet. Then the upper glass slide is carefully placed to squeeze the drop. The gap, δ, between the slides is controlled using three thin spacers. In our experiments the gap is kept constant at $\delta = 100 \pm 5$ µm. One can note that the presence of the spacers at the periphery of the cell does not affect the evaporation process of the drop and does not induce preferential deformation of the drop.

During the drying process, images of the drop are recorded at different times. The high contrast of the images allows an accurate detection of the drop edge and provides variations with time of the periphery length of the drop. The drying kinetics is obtained using a micro-scale (Sartorius) with a precision of 0.01 mg. The drying rate, $\frac{dm}{dt}$, is calculated from mass loss, m, as a function of time, t. Fluorescence microscopy has been investigated in order to detect the particles volume fraction inside the drop at successive times. The volume fraction of particles is deduced from a calibration curve between the fluorescence light received and a reference volume fraction [18]. At the beginning of the drying process, fluorescence intensity is homogeneous far from the border as shown in Fig. 2a (due to the presence of the menisci, the particles accumulate towards the drop edge which results in a high fluorescent intensity there). The intensity profile is expected to be proportional to the total amount of colloid in the drop, assuming the volume fraction is uniform in the vertical direction. As a result fluorescent intensity has been measured in the center of the profile for a given volume fraction ϕ^{fluo}. The ϕ^{fluo} dependence of the intensity I is linear as shown in Fig. 2b. The domain of validity of the calibration curve is restricted to $\phi^{fluo} < 5\%$ as for high ϕ^{fluo} value, the intensity I deviates from the linear relation because of the absorption of light. In our experiments the initial volume fraction of the colloidal particles expresses as: $\phi_0 = \phi^{disp} + \phi^{fluo}$, where ϕ^{disp} denotes the volume fraction of the non-fluorescent colloidal particles.

3. Results

3.1. Case of a pure water drop

In the ideal case of ultra pure solvents the drop completely evaporates as gas diffusion proceeds from the edge of the drop towards the edge of the cell and the drop shrinks isotropically [16]. Fig. 3 shows the time variation of the drying rate, $\frac{dm}{dt}$, for a drop of water. Since the distance, $R_s - R(t)$, over which the vapor that escapes from the drop interface and diffuses towards the cell edge, increases with time, the drying rate decreases. The evaporation rate, V_E, is defined as the gas flux at the drop interface, for a drop of radius R, as: $V_E = -\frac{1}{\nu_L}\frac{dR}{dt}$, where ν_L is the molecular volume of the liquid phase. V_E is related to the drying rate by: $\frac{dm}{dt} = -S(t)\nu_L\rho_L V_E$, where ρ_L is the density of the liquid, and $S(t) = 2\pi R(t)\delta$ is approximately the gas–liquid exchange surface. As a result it comes:

$$\frac{dm}{dt} = 2\pi\delta\rho_L R(t)\frac{dR}{dt} \tag{1}$$

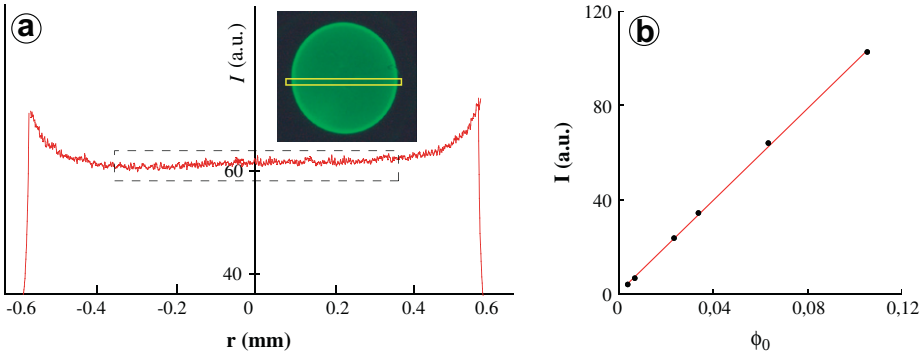

Fig. 2. (a) Fluorescence intensity profile, I, in arbitrary units as a function of the initial volume fraction, ϕ_0, of the dispersion. Measurements done across the bright rectangular region of interest in the fluorescent drop (insert). (b) Calibration curve of the fluorescence response: mean value of the fluorescence intensity measured in the dashed rectangular region in (a) vs. ϕ_0.

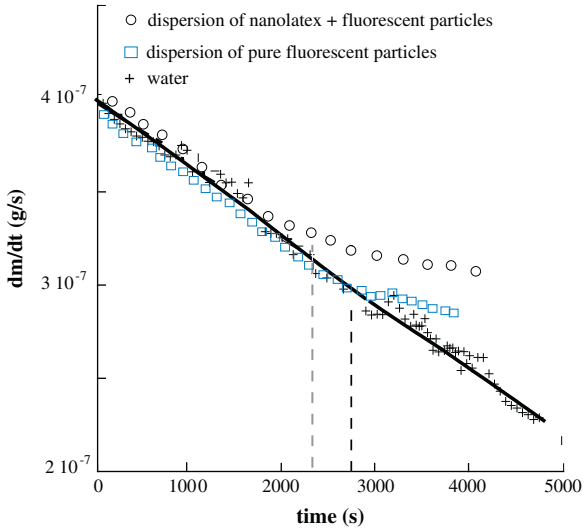

Fig. 3. Drying rate, dm/dt, as a function of time for three confined droplets. The drying rate was calculated from measurements of the mass variations versus time. The black line corresponds to the theoretical drying rate resulting from relation 1. Vertical dashed lines mark the discrepancy in time variation of the drying rate between dispersion drop and water drop.

Eq. (1) can be expressed as: $m(t) = m_0 + \pi\delta\rho_L(R^2(t) - R_0^2)$, where m_0 is the initial mass of the drop. Measurements of the drying rate (also the time variations of the drop radius $R(t)$ not shown here) are well fitted by Eq. (1) as shown in Fig. 3.

3.2. Case of a drop of a colloidal dispersion

At the beginning of the drying, nonvolatile compounds are advected to the evaporation surface due to the radial flow. This radial flow is induced by the evaporation rate, V_E, that gives the typical velocity scale characterizing the transport of particles. As a result a Péclet number, Pe, can be defined as the diffusion time, $t_D = \frac{R_0^2}{D_0}$, divided by the evaporation time, $t_E = \frac{R_s}{V_E^0}$, as follows: $Pe = \frac{R_0^2 V_E^0}{R_s D_0}$, with the diffusion coefficient $D_0 = \frac{k_B T}{6\pi\eta a} = 8.5 \times 10^{-12}$ m^2 s^{-1} using the Stokes–Einstein relation. In our experimental conditions: $10 < Pe < 100$. Moreover the concentration profile is expected to develop in a typical length scale $\xi = \frac{D_0}{V_E} \sim 100$ µm. Under these conditions, the transport of particles to the drop-air interface strongly suggests the formation of a porous skin during the drying process. This skin thickens due to the particle accumulation: the solvent evacuation is assumed to be driven by permeation through the porous skin. Consequently the evolution of the drop shape is induced by the solvent loss as shown in Fig. 4.

In a first stage, as the drop shrinks, it keeps a circular shape (Fig. 4a and b): its periphery length decreases steadily with time (see graph in Fig. 4). Then, contrasting with the case of a pure solvent, the droplet stops shrinking isotropically. A sudden inversion of curvature occurs and exhibits a buckling instability at time t_B (image in Fig. 4c and graph in Fig. 4). For $t > t_B$, the mean distance between the drop interface and the cell edge keeps constant. As a consequence the drying rate becomes roughly constant and deviates from the case of a pure solvent drop as shown in Fig. 3. The distortion is continued by an invagination tip that deepens with time (Fig. 4d). As a result the periphery length starts increasing (graph in Fig. 4). The same behavior is achieved for dispersion of pure fluorescent particles and binary mixture of fluorescent and nanolatex particles.

In the isotropic shrinkage stage (at time $t < t_B$), concentration profiles inside a drop of pure fluorescent particles have been plotted for different times t in Fig. 5.

Concentration profiles inside a drop of pure fluorescent particles have been plotted in Fig. 6 and in a drop of a binary mixture of fluorescent and nanolatex particles in Fig. 7. In each systems

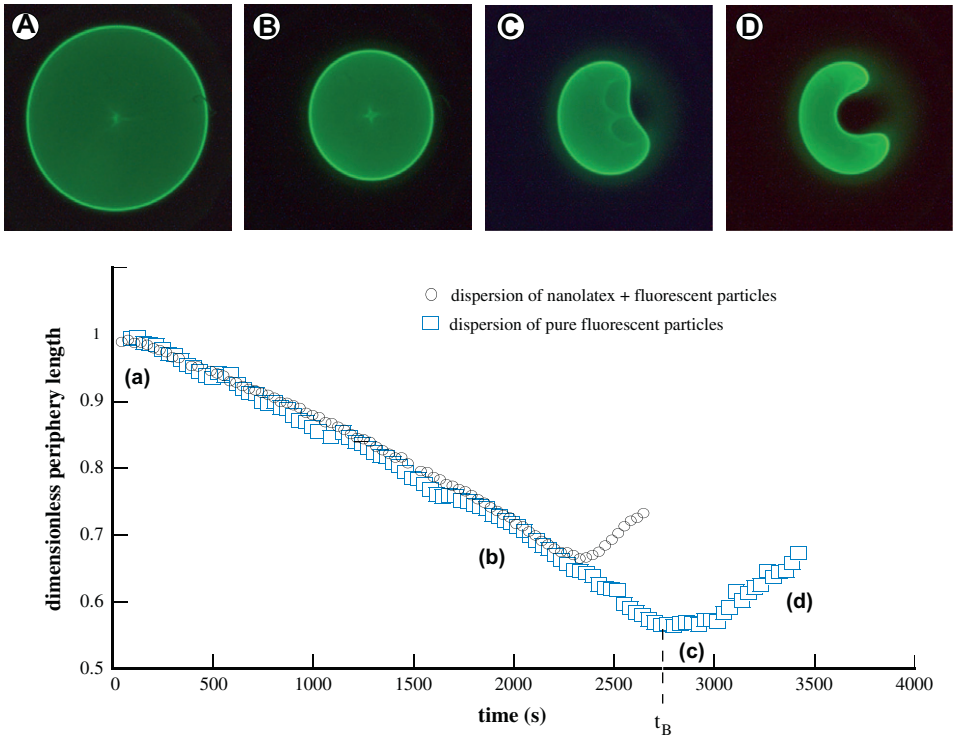

Fig. 4. (A–D) Digitized images taken during the deformation of a colloidal drop of fluorescent particles ($R_s = 10$ mm, $R_0 = 4$ mm). Graph: periphery length as a function of time for a dispersion of pure fluorescent particles and for a dispersion of both fluorescent and nanolatex particles. (For interpretation of the references to color in this figure legend, the reader is referred to the web version of this article.)

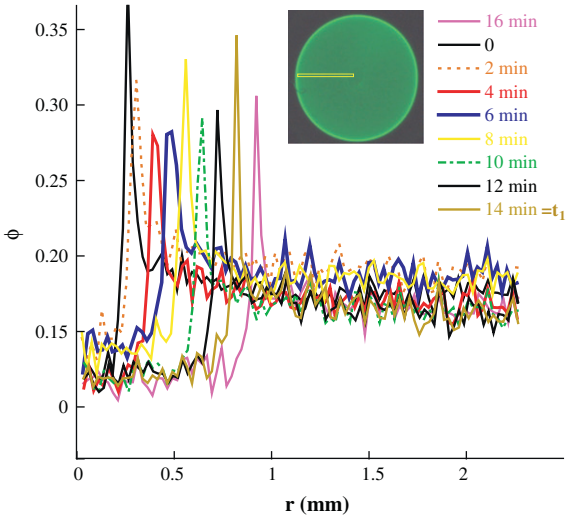

Fig. 5. Concentration profiles in the liquid phase for different time steps (bright rectangular region of interest in insert); curves have been smoothed for clarity ($R_s = 10$ mm, $R_0 = 4$ mm, $\phi_0 = 0.25$).

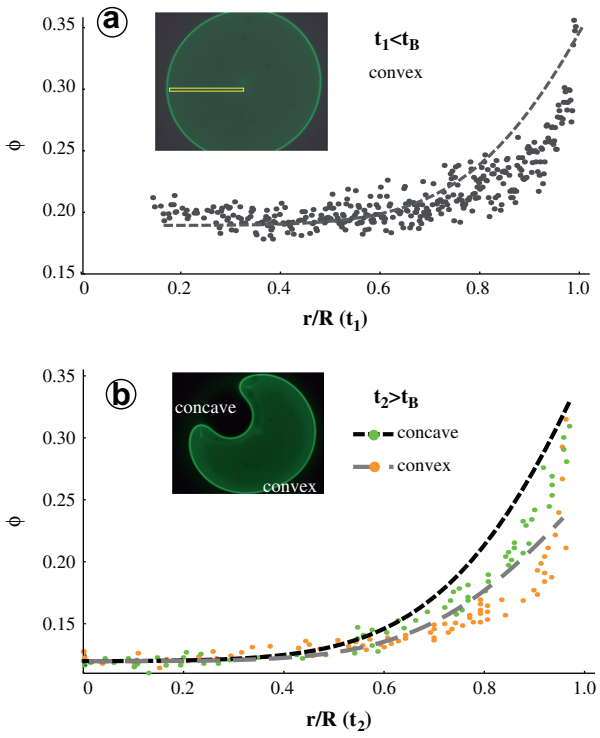

Fig. 6. Concentration profiles along a radius (bright rectangular region of interest) of a colloidal drop of pure fluorescent particles ($R_s = 10$ mm, $R_0 = 4$ mm, $\phi_0 = 0.25$). The plots are deduced from measurements by fluorescence microscopy and calibration related to Fig. 2. (a) Concentration profile in a circular drop at time t_1 such as $t_1/t_B = 0.7$. (b) Concentration profile in a distorted drop at time t_2 such as $t_2/t_B = 1.2$. Dashed lines are fits obtained by solving Eq. (2) using a constant diffusion coefficient $D(\phi) = D_0$. (For interpretation of the references to color in this figure legend, the reader is referred to the web version of this article.)

two time steps have been considered: in the isotopic shrinkage stage (at time $t_1 < t_B$) and in the distortion stage (at time $t_2 > t_B$).

- At time t_1, when the drop shape is still circular, ϕ is homogeneous near the center of the drop and increases when approaching the drop periphery (Fig. 6a and 7a).

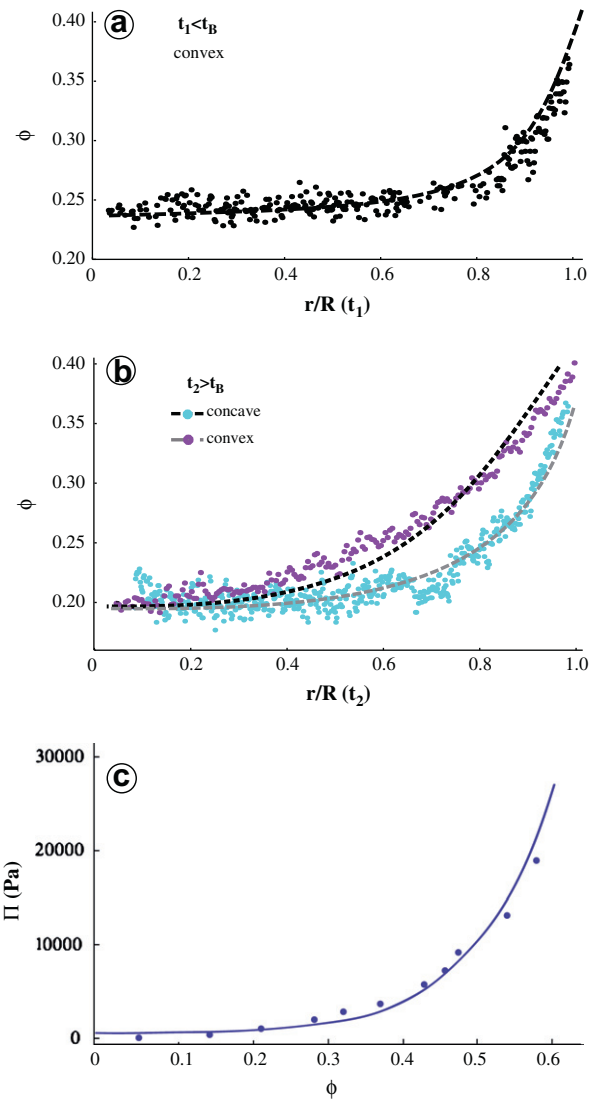

Fig. 7. Concentration profiles along a radius of a colloidal drop of a binary mixture of fluorescent and nanolatex particles ($R_s = 10$ mm, $R_0 = 4.1$ mm, $\phi_0 = 0.25$). (a) Concentration profile in a circular drop at time t_1 such as $t_1/t_B = 0.7$. (b) Concentration profile in a distorted drop at time t_2 such as $t_2/t_B = 1.2$. Experimental profiles are well fitted by solving Eq. (2) with a collective-diffusion coefficient $D_c(\phi)$ (dashed lines). (c) Variation of the osmotic pressure, Π, with the particle volume fraction, ϕ, for a Latex dispersion (particle size =10 nm); experimental data $\Pi(\phi)$ come from reference [13,14].

- At time t_2 the drop is distorted leading to concave and convex interfaces. Measurements reveal a lower concentration profile near the concave interface than near the convex one (Fig. 6b and 7b).

Quantifying these observations allow us to estimate the evaporation rates through both convex and concave interfaces that drive these concentration profiles. In this way, the concentration profile can be quantified by the following diffusion equation of $\phi(r,t)$ [19]:

$$\frac{\partial \phi}{\partial t} = \frac{1}{r}\frac{\partial}{\partial r}\left(rD(\phi)\frac{\partial \phi}{\partial r}\right) \tag{2}$$

where the diffusion coefficient $D(\phi)$ in general depends on ϕ. Boundary conditions on Eq. (2) are that the flux of particles at the liquid air-interface matches the recession due to evaporation, hence:

$$\left(D(\phi)\frac{\partial\phi}{\partial r}\right)_{r=R(t)} = V_E\phi_{r=R(t)} \quad (3)$$

also the concentration at the drop center, $\phi(0,t)$, plays the role of a parameter directly deduced from the concentration profile measured at $r=0$ at time t.

Two cases can be highlighted: $D(\phi)=D_0$ where the Stokes–Einstein diffusion coefficient is independent of ϕ and $D(\phi)=D_c(\phi)$ where $D_c(\phi)$ denotes the collective diffusion coefficient that depends on the particles volume fraction. In the last case, the collective diffusion coefficient rapidly increases when approaching the close-packing volume fraction, ϕ_g [17]. $D_c(\phi)$ describes the interactions between the colloidal particles on the solvent transport [21]. Thus, $D_c(\phi)$ is proportional to the osmotic pressure gradient as [22]: $D_c(\phi)=\frac{K(\phi)}{6\pi\eta a}V_p\frac{\partial\Pi}{\partial\phi}$, where Π is the osmotic pressure, V_p is the volume of the suspended particle and $K(\phi)$ denotes the sedimentation coefficient that describes the hydrodynamic interactions at finite concentration [15]. The osmotic pressure expresses as:

$$\Pi(\phi)=\frac{k_BT}{V_p}\phi Z(\phi) \quad (4)$$

where k_B is the Boltzmann constant, T is the absolute temperature and $Z(\phi)$ the osmotic compressibility of the colloidal dispersion accounting for the effect of particle–particle interactions on the osmotic pressure. An analytical formula derived by Peppin et al. [20] for $Z(\phi)$ expresses as: $Z(\phi)=\frac{1+a_1\phi+a_2\phi^2+a_3\phi^3+a_4\phi^4}{1-\frac{\phi}{\phi_g}}$, with $a_1=4-1/\phi_g$, $a_2=10-4/\phi_g, a_3=18-10/\phi_g, a_4=1.85\phi_g^5-18/\phi_g$.

Eq. (2) is resolved numerically with a Runge–Kutta numerical scheme in the case of circular drops, using the boundary conditions, the initial particle volume fraction of the dispersion being ϕ_0. In the case of distorted drops, we assume that Eq. (2) allows us to obtain a valid concentration profile along a radius of the drop, without angular dependence.

In the case I, we consider a drop of pure fluorescent particles the variation of the osmotic pressure with the volume fraction in unknown; also we fit the experimental concentration profile by the local variation of ϕ obtained using Eq. (2) and the constant diffusion coefficient D_0. At time t_1, we expect that the evaporation rate at the drop-air interface is constant since the drop is circular. The evaporation rate in Eq. (3) is deduced from the time variation of the drying rate in Fig. 3 at time $t_1/t_B=0.7 : V_E(t_1)=(1.7\pm0.2)\times 10^{-7}$ m s^{-1}. This leads to the approximate adjustment in Fig. 6a. However at time t_2 such as $t_2/t_B=1.2$, due to the strong distortion of the drop, we expect that the evaporation rate is not uniform along the drop interface and depend on the concave and convex interfaces of the drop. The approximate adjustment of the experimental concentration profile in Fig. 6b need V_E as a free parameter. Particularly the best fit with the experimental data gives: $V_E^{convex}(t_2)=(1.5\pm0.2)\times10^{-7}$ m s^{-1} near the convex interface and $V_E^{concave}(t_2)=(0.8\pm0.2)\times10^{-7}$ m s^{-1} near the concave interface.

In the case II, we consider now the case of the colloidal drop of a binary mixture of pure fluorescent and nanolatex particles. The volume fraction of dispersion of fluorescent particles play the role of probes in the colloidal dispersion and is low in comparison with the volume fraction of nanolatex particles (volume fraction in fluorescent particles is 0.5% and the initial particle volume fraction in the dispersion is 25%). The concentration profiles can be quantified using the local variation of ϕ obtained using Eq. (2) and, this time, the collective diffusion coefficient $D_c(\phi)$. Indeed, the variation of the osmotic pressure with the volume fraction for the dispersion of nanolatex particles is plotted in Fig. 7c [13,14]. The fit corresponds to the prediction of the osmotic pressure of the dispersion using Eq. 4. Assuming that the fluorescent particles do not strongly modify the osmotic pressure of the dispersion, the concentration profiles have been fitted for $t_1/t_B=0.7$ in Fig. 7a and $t_2/t_B=1.2$ in Fig. 7b. As in the case I, for the circular drop, no free parameter is needed and the evaporation rate at time t_1 is deduced from Fig. 3. For distorted drop, the best fit with the experimental data gives: $V_E^{convex}(t_2)=(1.6\pm0.2)\times10^{-7}$ m s^{-1} near the convex interface and $V_E^{concave}(t_2)=(0.7\pm0.2)\times10^{-7}$ m s^{-1} near the concave interface. Good agreement between theory and measurements in Figs. 6 and 7 reveal that the effect of the particles interaction, described by the collective-diffusion coefficient $D_c(\phi)$, is to sharpen the volume fraction profile near the drop interface.

The higher value for V_E^{convex} comparing to $V_E^{concave}$ can be interpreted as follows: the air located inside the invagination tip becomes quickly saturated in water vapor and therefore slowing down the evacuation of the vapor from the drop interface; as a result it is easier to evaporate in the convex region than in the concave one.

Finally high fluorescence intensity is detected near high curvature regions as shown in the three-dimensional plot obtained by Image-processing in Fig. 8a. The sketch in Fig. 8b shows three main regions in the evaporation process: convex interface, concave interface where the evaporation is lower, and interface of high curvature denoted by "wedges". As for $V_E^{concave}$, an estimation of the evaporation rate at these locations can be made and yields to: $V_E^{wedge}=(1.2\pm0.2)\times10^{-7}$ m s^{-1}. Basically in a distorted drop, the drying rate involves three main contributions as described in the sketch 8b. These contributions are driven by evaporation through

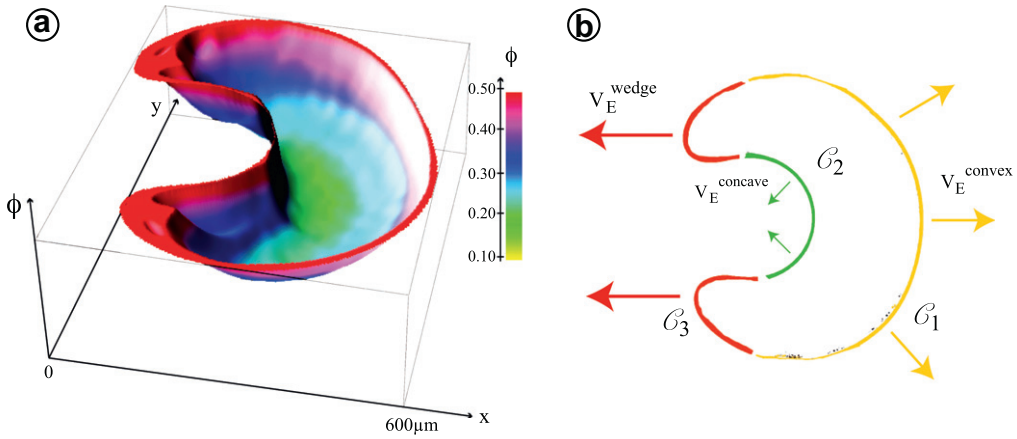

Fig. 8. (a) Three-dimensional profile obtained by image-processing (ImageJ) from a digitized image obtained in fluorescent microscopy. (b) Sketch showing three drop/air interfaces of various interface curvatures. $\mathcal{C}_1$ denotes the convex region while $\mathcal{C}_2$ denotes the concave one; $\mathcal{C}_3$ denotes the wedge interface.

concave $\mathcal{C}_1$, convex $\mathcal{C}_2$ and wedge interface $\mathcal{C}_3$. The deduced drying rate is then:

$$v_L\delta\rho\left(\int_{\mathcal{C}_1} V_E^{convex}dl+\int_{\mathcal{C}_2} V_E^{concave}dl+\int_{\mathcal{C}_3} V_E^{wedge}dl\right) = (1.2\pm 0.3)\times 10^{-7}\ \mathrm{g\ s^{-1}}$$

This consideration based on conservation at the drop–air interface is in agreement with the experimental value deduced from Fig. 4c: $\frac{dm}{dt}|_{t_2} = 2.7\times 10^{-7}$ g s^{-1}, in accordance with Eq. (1). As a consequence, coupling measurements of fluorescence microscopy with the diffusion model highlights a non-uniform evaporation rate at the distorted drop/air interface.

4. Conclusion

Drying process of a drop of a colloidal dispersion in a confined geometry yields to high distortions in the shape of the drop that tends to modify the particles distribution inside the drop. The first stage of the drying process is similar to the case of a pure solvent drop: the drop starts shrinking as water evaporates, then the transport of particles to the drop periphery results in the formation of a porous skin. The porous skin buckles under the action of the capillary forces inside the porous envelope. Particularly the time for buckling depends on both the drying kinetics and the initial concentration of colloidal dispersion. After the buckling process, the evaporation rate keeps constant and diffusion of solvent happens through the skin. The drop shape is circular before the buckling process and after it becomes asymmetric as the initial depression inside the drop is proceeded. The single depression continues in the formation of an invagination tip that deepens inside the drop. This generates strong distortions of the drop shape and results in both concave and convex interfaces. Fluorescence microscopy measurements highlight different concentration gradients inside the drop near convex and concave interfaces. This supposes preferential transport of particles inside the drying drop; particles are actually less easily advected out of concave regions than convex ones where evaporation is not limited. The influence of the initial particle volume fraction and the initial evaporation rate on the concentration profile in the drops (circular or distorted case) is investigated through fluorescence microscopy measurements. These experimental data can be well fitted by a convection–diffusion model taking into account a collective diffusion coefficient. Moreover the preferential transport of particles suggests the formation of a non-uniform envelope in thickness: the envelope remains thin in concave region as it thickens in the convex one [8]. As the envelope is nonuniform, one expected that only one depression can deep inside the drop during water loss.

Acknowledgments

The authors thank E. Sultan and M. Ding for discussions and experimental help. We thank A. Aubertin, L. Auffray, C. Borget and R. Pidoux for the experiment engineering and technical improvements.

References

[1] Z. Mitov, E. Kumacheva, Phys. Rev. Lett. 81 (1998) 3427.
[2] H. Wang, Z. Wang, L. Huang, A. Mitra, Y. Yan, Langmuir 17 (2001) 2572.
[3] P.G. de Gennes, Eur. Phys. J. E (2001) 421.
[4] N. Bassou, Y. Rharbi, Langmuir (2009) 25.
[5] T. Okuzono, K. Ozawa, M. Doi, Phys. Rev. Lett. 97 (2006) 136103–136106.
[6] L. Pauchard, F. Parisse, C. Allain, Phys. Rev. E 59 (1999) 3737.
[7] L. Pauchard, C. Allain, Europhys. Lett. 62 (2003) 897–903.
[8] L. Pauchard, Y. Couder, Europhys. Lett. 66 (5) (2004) 667.
[9] N. Tsapis, E.R. Dufresne, S.S. Sinha, C.S. Riera, J.W. Hutchinson, L. Mahadevan, D.A. Weitz, Phys. Rev. Lett. 94 (2005) 018302.
[10] J. Leng, Phys. Rev. E 82 (2010) 021405.
[11] L. Pauchard, M. Mermet-Guyennet, F. Giorgiutti-Dauphiné, Chem. Eng. Process. 94 (2011) 483.
[12] F. Boulogne, F. Giorgiutti-Dauphiné, L. Pauchard, Soft Matter, in press. doi:10.1039/C2SM26530C.
[13] B. Espinasse, Approche théorique et expérimentale de la filtration tangentielle de colloïdes: flux critique et colmatage, Ph.D. thesis, Université Paul Sabatier, Toulouse III, 2003.
[14] The osmotic stress technique is based on water exchange between the colloidal dispersion and a reservoir of known osmotic pressure. The sample is placed in a dialysis bag which is immersed in a reservoir that contains a solute (polymer) for which the relation between osmotic pressure and concentration is known. The solvent, i.e. water, ions and small organic molecules can exchange between both compartments. At equilibrium, the chemical potentials of water and salt on either side of the membrane are equal, and therefore the osmotic pressure of the sample equals that of the polymer in the reservoir.
[15] W.B. Russel, D.A. Saville, W.R. Schowalter, Colloidal Dispersions, Cambridge University Press, 1989.
[16] F. Clément, J. Leng, Langmuir 20 (2004) 6538.
[17] L. Daubersies, J.B. Salmon, Phys. Rev. E 84 (2011) 031406.
[18] T. Kajiya, D. Kaneko, M. Doi, Langmuir 24 (2008) 12369–12374.
[19] A.F. Routh, W.B. Zimmerman, Chem. Eng. Sci. 59 (2004) 2961.
[20] S.S.L. Peppin, J.A.W. Elliott, M.G. Worster, J. Fluid. Mech. 554 (2006) 147–166.
[21] P. Bacchin, D. Si-Hassen, V. Starov, M.J. Clifton, P. Aimar, Chem. Eng. Sci. 57 (2002) 77–91.
[22] A. Einstein, Investigation on the Theory of the Brownian Movement, Dover Publications, New York, 1956.